Giant Magneto-Optical Effect in van der Waals Room-Temperature Ferromagnet Fe_3GaTe_2

Xiaomin Zhang(张晓敏)[1,2], Jian Wang(王健)[1,2], Wenkai Zhu(朱文凯)[1], Jiaqian Zhang(张佳茜)[3], Weihao Li(李伟浩)[1,2], Jing Zhang(张菁)[1,2*], and Kaiyou Wang(王开友)[1,2*]

[1]*State Key Laboratory of Superlattices and Microstructures, Institute of Semiconductors, Chinese Academy of Sciences, Beijing 100083, China*
[2]*Center of Materials Science and Optoelectronics Engineering, University of Chinese Academy of Sciences, Beijing 100049, China*
[3] *School of Materials, Shenzhen Campus of Sun Yat-sen University, Shenzhen 518107, China*

(Received 8 April 2024; accepted manuscript online 24 May 2024)

The discovery of ferromagnetic two-dimensional (2D) van der Waals (vdWs) materials provides an opportunity to explore intriguing physics and to develop innovative spin electronic devices. However, the main challenge for practical applications of vdWs ferromagnetic crystals lies in the weak intrinsic ferromagnetism and small perpendicular magnetic anisotropy (PMA) above room temperature. Here, we report the intrinsic vdWs ferromagnetic crystal Fe_3GaTe_2, synthesized by the self-flux method, exhibiting a Curie temperature (T_C) of 370 K, a high saturation magnetization of 33.47 emu/g, and a large PMA energy density of approximately 4.17×10^5 J/m^3. Furthermore, the magneto-optical effect is systematically investigated in Fe_3GaTe_2. The doubly degenerate $E_{2g}(\Gamma)$ mode reverses the helicity of incident photons, indicating the existence of pseudoangular-momentum (PAM) and chirality. Meanwhile, the non-degenerate non-chiral $A_{1g}(\Gamma)$ phonon exhibits a significant magneto-Raman effect under an external out-of-plane magnetic field. These results lay the groundwork for studying phonon chirality and magneto-optical phenomena in 2D magnetic materials, providing the feasibility for further fundamental research and applications in spintronic devices.

DOI: 10.1088/0256-307X/41/6/067503

Since the intrinsic magnetism of bilayer $Cr_2Ge_2Te_6$ and monolayer CrI_3 was reported in 2017,[1,2] an increasing number of 2D magnetic materials have been discovered.[3–7] For high density spintronic devices, good perpendicular magnetic anisotropy with high Curie temperature is strongly desired. Therefore, many spintronic devices have been demonstrated based on strong PMA ferromagnet Fe_3GeTe_2.[8–15] However, its intrinsic T_C is only 220 K and well below room temperature, which cannot satisfy the application requirements. Various modulation methods have been adopted to enhance the T_C of 2D vdWs magnets, such as ionic gate doping,[1,6–18] shape and size effects,[19] interface spin-orbit coupling with topological insulators,[20] proximity effects with antiferromagnets,[21,22] and interlayer exchange coupling with ferromagnetic materials.[23] However, these approaches are hard to manipulate and remain challenging for practical applications of spintronic devices. Two-dimensional ferromagnetic materials with intrinsic T_C above room temperature are scarce. Recently, great efforts have been dedicated to finding intrinsic room-temperature 2D vdWs ferromagnetic materials. Materials such as Fe_5GeTe_2 with a T_C of 310 K,[24] 1T-$CrTe_2$ capable of operating at 300 K,[25] and Fe_3GaTe_2 with an ultrahigh T_C of 370 K have been successively discovered.[26] The finding of these materials provides an opportunity for manufacturing low-power, high-density and nonvolatile spintronic devices operating at room temperature.

Since its first discovery in 2022, Fe_3GaTe_2 has attracted widespread attention from researchers in the field of 2D magnetic materials due to its outstanding T_C and excellent perpendicular magnetic anisotropy. To date, $Fe_3GaTe_2/WSe_2/Fe_3GaTe_2$ magnetic tunnel junctions (MTJs) have been reported,[27] achieving a large tunneling magnetoresistance (TMR) of 85% at room temperature ($T = 300$ K). By constructing Pt/Fe_3GaTe_2 bilayer Hall devices, room temperature current-induced magnetization switch of Fe_3GaTe_2 was demonstrated with the assistance of a small external in-plane magnetic field.[28] Recently, it is reported that magnetoresistive memory devices can achieve all-electrical data reading and writing at room temperature based on $WTe_2/Fe_3GaTe_2/BN/Fe_3GaTe_2$ heterostructures.[29] Under an external magnetic field, magnetic skyrmions are generated through current pulses in Fe_3GaTe_2. The generation of skyrmions follows a thermal activation process and exhibits a current-induced skyrmion motion.[30] Despite plenty of progress on device applications, much of the underlying physics responsible for the emergence of new functionalities in this material, including chiral phonons, spin-phonon coupling, and magneto-optical effects, remain unexplored and require further investigation. The deep understanding of the chi-

*Corresponding author. Email: jzhang@semi.ac.cn; kywang@semi.ac.cn
© 2024 Chinese Physical Society and IOP Publishing Ltd

ral phonons in Fe_3GaTe_2 is highly desirable and potentially important for novel phenomena, such as phonon Hall effect,[31] topological states,[32] and chiral-phonon-activated spin Seebeck effect,[33] which could provide new strategy for designing next generation spintronic devices.

In this work, we synthesize a 2D vdWs ferromagnetic crystal Fe_3GaTe_2 using the self-flux method and systematically investigate its magnetic properties through various characterizations. The T_C of Fe_3GaTe_2 2D crystals is up to $\sim$370 K, with a high saturation magnetization (33.47 emu/g) and excellent perpendicular magnetic anisotropy (4.17×10^5 J/m^3 for bulk). Furthermore, we conduct systematic Raman measurements to study the lattice dynamics, chiral phonons, and giant magneto-optical effects in Fe_3GaTe_2. At room temperature, the $A_{1g}(\Gamma)$ and $E_{2g}(\Gamma)$ phonon modes can be observed, corresponding to the out-of-plane and in-plane vibrations. Our results indicate that the doubly degenerate $E_{2g}(\Gamma)$ mode alters the helicity of incident photons, thereby being described as chiral phonons in Fe_3GaTe_2. Beyond that, through co- and cross-linearly polarized Raman characterization at 1.7 K, we observed a transition in the linear polarization degree of the A_{1g} peak from 100% to -35% under magnetic field ranging from 0 T to 5 T, demonstrating the giant magneto-optical effect in Fe_3GaTe_2.

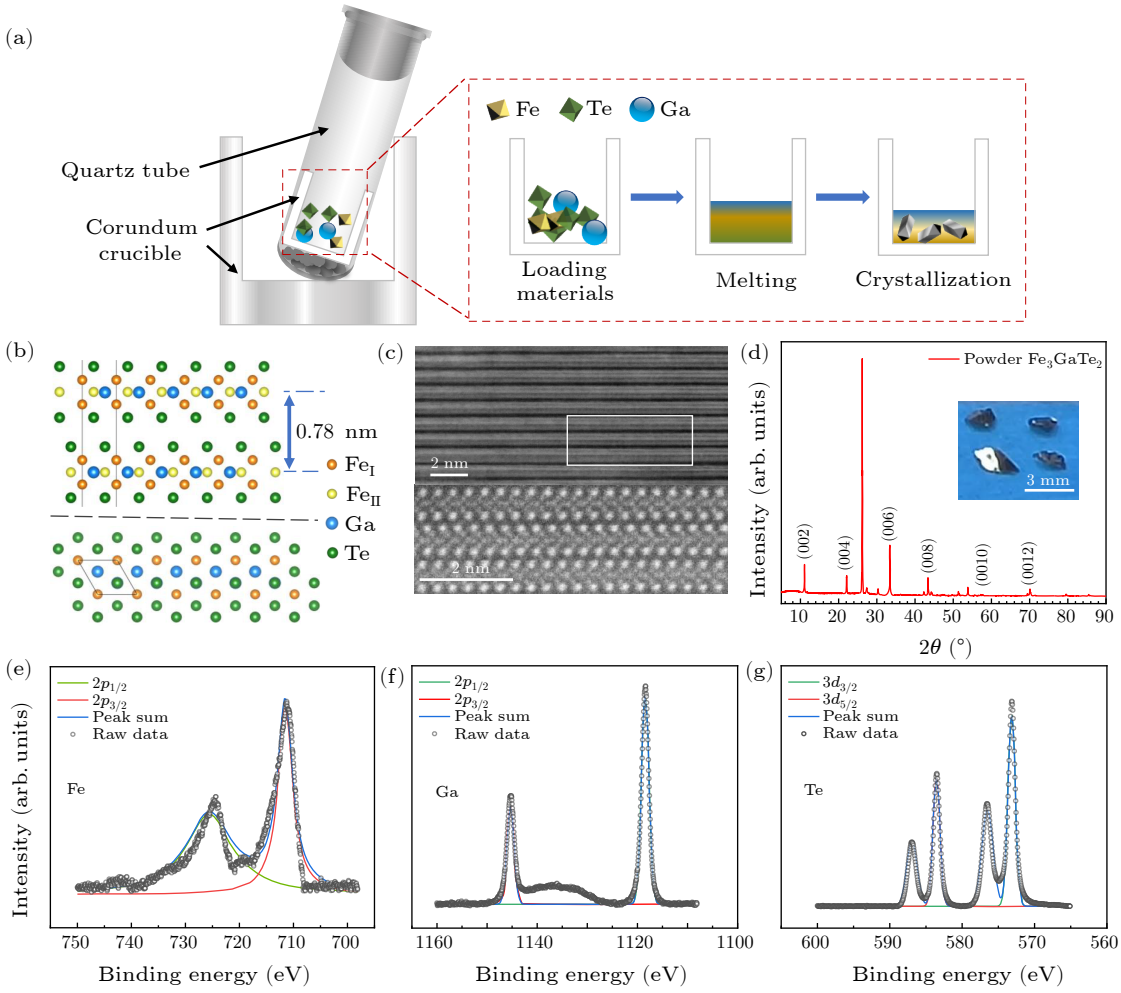

Fig. 1. Growth method and characterization of Fe_3GaTe_2. (a) Setup for self-flux growth. The evolution of precursors inside the alumina crucible during the growth process (highlighted in dashed red box). (b) Crystal structure of Fe_3GaTe_2 viewed from the side (top) and from the top (bottom). (c) High-resolution cross-sectional HAADF-STEM image of exfoliated Fe_3GaTe_2 nanoflakes (top), zoomed-in image showing atomic arrangement (bottom). (d) Experimental XRD spectrum of the Fe_3GaTe_2 bulk crystal. Inset: Optical image of a typical bulk crystal. Scale bar: 3 mm. (e)–(g) XPS analysis of (e) Fe, (f) Ga, (g) Te of the exfoliated fresh Fe_3GaTe_2 crystal.

The Fe_3GaTe_2 single crystals were grown using the self-flux method. High-purity Fe powders (Aladdin, 99.95%), Ga grains (Aladdin, 99.9999%), and Te powders (Aladdin, 99.99%) were mixed in a molar ratio of 1 : 1 : 2 and placed in a corundum crucible, which was then encapsulated in a quartz tube, as shown in Fig. 1(a). The quartz tube was heated to 1273 K over a period of 1 h and maintained at this temperature for 24 h to melt the precursor materials. Subsequently, it was rapidly cooled to 1153 K and then slowly cooled to 1053 K at a rate of 1 °C per hour. Af-

ter that, the sample was naturally cooled down to room temperature. The crystal size typically is ranging from 2 mm to 3 mm, as illustrated in the inset of Fig. 1(d). The crystal structure and atomic arrangement of Fe_3GaTe_2 are shown in Fig. 1(b). Fe_3GaTe_2 exhibits a hexagonal structure with the space group $P6_3/mmc$ ($a = b = 3.9860$ Å, $c = 16.2290$ Å, $\alpha = \beta = 90°$, $\gamma = 120°$). We characterized the atomic structure of exfoliated Fe_3GaTe_2 sample using cross-sectional high-angle annular dark-field scanning transmission electron microscopy (HAADF-STEM). Figure 1(c) displays the highly crystalline structure and atomic arrangement of layered Fe_3GaTe_2. Each layer of Fe_3GaTe_2 consists of alternating Te–Fe–Ga (Fe)–Fe–Te atomic planes, exhibiting clear atomic boundaries without any noticeable atomic mixing or defects. The thickness of a single layer of Fe_3GaTe_2 is approximately 0.78 nm. In Fig. 1(d), powder x-ray diffraction (XRD) of the as-grown bulk Fe_3GaTe_2 exhibits a typical $(00l)$ orientation, with extremely narrow full width at half maximum (0.08°), indicating high crystallinity of the as-grown materials. Freshly exfoliated Fe_3GaTe_2 crystals were measured using x-ray photoelectron spectroscopy (XPS). The XPS spectra of Fe, Ga, and Te in the Fe_3GaTe_2 crystal are shown in Figs. 1(e)–1(g). In Fig. 1(e), two peaks at binding energies of 710.8 eV and 724.4 eV correspond to Fe $2p_{3/2}$ and Fe $2p_{1/2}$ in the Fe_3GaTe_2. Additionally, in Fig. 1(f), the binding energies of Ga $2p_{3/2}$ and Ga $2p_{1/2}$ are observed at 1117.6 eV and 1144.5 eV, respectively. Similarly, in Fig.1(g), the binding energies of Te $3d_{5/2}$ and Te $3d_{3/2}$ are found to be 572.8 eV and 583.2 eV, respectively.

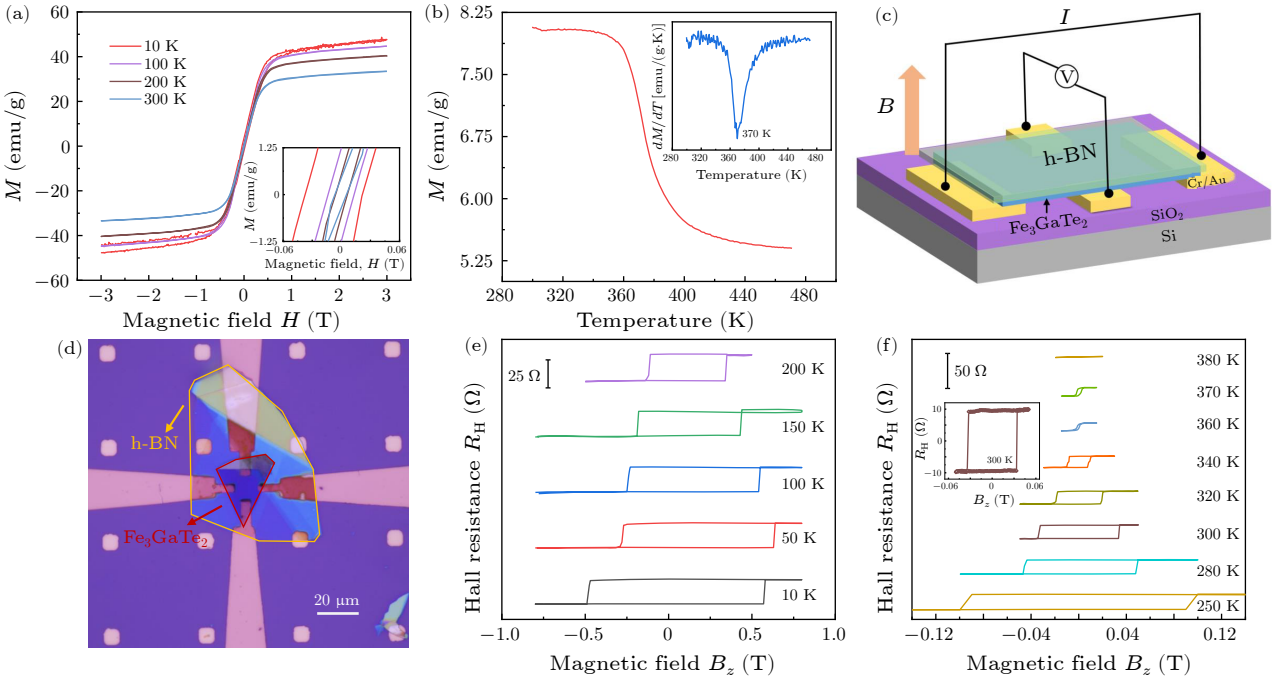

Fig. 2. Magnetization measurements of bulk Fe_3GaTe_2 and anomalous Hall effect (AHE) in few-layer Fe_3GaTe_2. (a) M–H curves of bulk Fe_3GaTe_2 crystals at different temperatures with magnetic fields along the out-of-plane direction. The inset in (a) shows the enlarged image of hysteresis loops. (b) Field-cooling curve of the Fe_3GaTe_2 bulk crystal ($B = 0.1$ T, out-of-plane direction). The inset shows the differential result of the curve. (c) Schematic of the device structure and Hall measurements. (d) Optical image of the FGT/h-BN sample. The scale bar is 20 μm. (e)–(f) Hall resistance R_H as a function of external perpendicular magnetic field at different temperatures. The inset in (f) is the enlarged image of the hysteresis loop at 300 K.

Magnetic measurements of the Fe_3GaTe_2 bulk sample were conducted using a superconducting quantum interference device (SQUID). As shown in Fig. 2(a), typical magnetic field-dependent M–H hysteresis loops at different temperatures (10 K, 100 K, 200 K, and 300 K) were measured under an out-plane magnetic field, confirming the room-temperature ferromagnetism of the Fe_3GaTe_2. The extracted saturation magnetization is 33.47 emu/g and large PMA energy density is up to 4.17×10^5 J/m^3 at 300 K for the bulk Fe_3GaTe_2. Field-cooling measurement from 470 K to 300 K under an out-of-plane magnetic field at 0.1 T demonstrates the typical ferromagnetic behavior of the bulk Fe_3GaTe_2, as depicted in Fig. 2(b). The inset of Fig. 2(b), obtained by differentiating the curve, reveals T_C of approximately 370 K for the Fe_3GaTe_2. Figure 2(c) illustrates the schematic diagram of the device structure of Hall measurement. Under the perpendicular external magnetic field B, the Hall resistance R_H is achieved by dividing the measured Hall voltage V_H by the applied channel current (10 μA). The optical microscope image of the device is shown in Fig. 2(d). We employed a dry transfer technique to stack the exfoliated few-layer Fe_3GaTe_2 (about 10 nm) onto Cr/Au electrodes (10/40 nm). The electrodes were patterned using photolithography, sputter deposition, and lift-off processes on a SiO_2/Si substrate. Boron nitride was utilized to encapsulate and protect the Fe_3GaTe_2 sur-

face against oxidation. We utilized a CRX-VF cryogenic probing station (Lake Shore Cryotronics, Inc.) to measure the Hall resistance $R_{\rm H}$ hysteresis loops at different temperatures ranging from 10 K to 380 K shown in Figs. 2(e)–2(f). The hysteresis loop of the sample exhibits asymmetric behavior at low temperatures, which is related to many factors. The coercivity field is not an intrinsic physical quantity, influenced by the geometric shape, thickness, uniformity, and defects of the sample, which has been observed in 2D vdWs materials.[14,34] At 300 K, the device exhibits a perfect square-shaped hysteresis loop with a coercive field $H_{\rm C}$ of $\sim$335 Oe, indicating the strong PMA of Fe_3GaTe_2. Due to the increased thermal fluctuations, the coercive field $H_{\rm C}$ decreases with increasing temperature and eventually disappears above $T_{\rm C}$.

Polar reflective magnetic circular dichroism (RMCD) spectroscopy is a non-destructive and effective technique for probing 2D magnet.[2,35,36] It measures the different absorption of left and right circularly polarized light induced by the out-of-plane magnetization of the magnetic materials (parallel to the light propagation). The RMCD measurement was conducted in a closed-cycle helium cryostat system (attoDRY2100) with an out-of-plane magnetic field reaching up to 9 T, covering a temperature range from 1.7 K to 300 K. A 532 nm laser with power of about 0.5 μW was used. We performed RMCD measurements on Fe_3GaTe_2 samples with different layer numbers, labeled with P1 and P2, as shown in Fig. 3(a). Atomic force microscopy (AFM) measurements on the same flake were carried out to confirm the sample thickness, with 10 nm and 50 nm for P1 and P2, respectively.

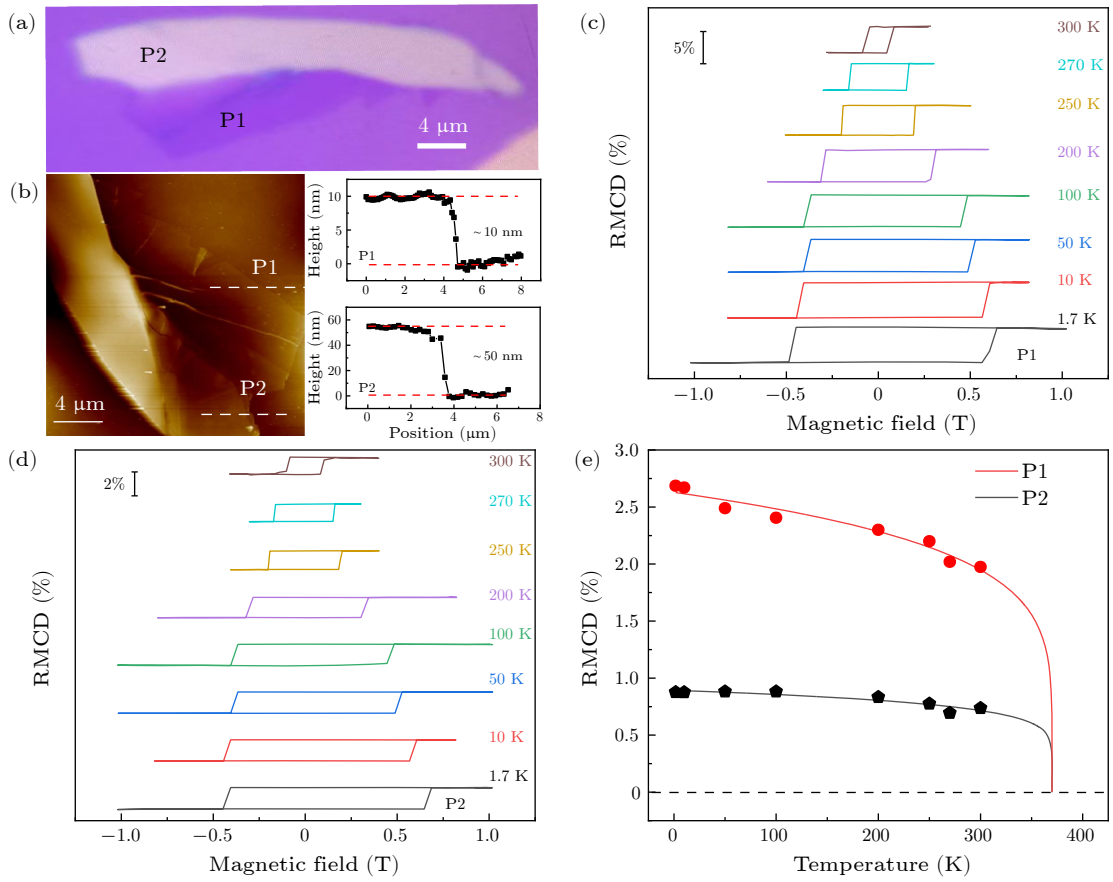

Fig. 3. RMCD characterizations of Fe_3GaTe_2 flakes. (a) Optical microscope image of the samples, with positions 1 and 2 as indicated in the picture. (b) AFM image of Fe_3GaTe_2 (left). Height distribution along the white dashed lines at positions P1 (top right) and P2 (bottom right). The scale bar in the image is 4 μm. RMCD signals as a function of magnetic field at different temperatures at position P1 (c) and position P2 (d). (e) Residual RMCD values as a function of temperature at positions P1 (circles) and P2 (pentagons). The straight lines represent the temperature dependence of the residual RMCD fitted according to the formula.

The relationship between the RMCD intensity and the magnetic field at different temperatures for the two samples is shown in Figs. 3(c) and 3(d). It can be observed that when the temperature ranges from 1.7 K to 300 K, both the samples exhibit rectangular hysteresis loops, further indicating strong perpendicular magnetic anisotropy and a $T_{\rm C}$ exceeding room temperature. To determine the $T_{\rm C}$ of the material, as shown in Fig. 3(e), we extracted the residual RMCD signal at each temperature and fitted the $T_{\rm C}$ of the material following the power-law equation

$$M(T) = M_0 \left(1 - \frac{T}{T_{\rm C}}\right)^{\beta}, \tag{1}$$

where β is the critical exponent associated with the spontaneous magnetization (e.g., $\beta = 3/8$ for the 3D Ising model and $\beta = 1/8$ for the 2D Ising model),[37] M_0 is the magnetization value at 0 K. The extracted T_C of the sample P1 is approximately 370 K and β is about 0.179, confirming the 2D Ising magnetism model in few-layer Fe_3GaTe_2. Note that β from RMCD is also consistent with the previous AHE measurement results (the fitted T_C is 372 K and β is 0.168). The typical RMCD values for common 2D magnetic materials usually fall in the range from 0.1% to 1%.[35,38] The thicker Fe_3GaTe_2 sample has an RMCD value of 1%, while the 10-nm-thick sample exhibits a larger RMCD signal, up to 2%, indicating excellent magnetic properties of the material, possibly because the reduced electronic screening in thinner samples enhances the exchange coupling,[39] which has also been directly observed in Fe_3GaTe_2 flakes or other 2D vdWs magnets.[26,40,41] It can also be learnt that the coercivity of the two samples shows no significant difference, presenting the decreasing trend because of the effect of thermal fluctuations when the temperature increases.

In a magnetic system, phonon have nonzero angular momentum, leading to phonon angular momentum and the chiral phonons. In order to determine the phonon chirality of Fe_3GaTe_2, we performed Raman spectra with both linearly and circularly polarized configuration at 2.33 eV excitation. Fe_3GaTe_2 has a hexagonal structure of space group $P6_3/mmc$.[26] According to group theory, it has three active Raman modes, perpendicular A_{1g}, in-plane E_{1g} and E_{2g}. E_{1g} and E_{2g} phonon modes are doubly degenerate and E_{1g} is normally forbidden. Figure 4(a) is the typical phonon dispersion band structure of few-layer Fe_3GeTe_2 by first-principles calculation. The phonon mode branches of A_{1g} and E_{2g} are at about 151 cm^{-1} and 112 cm^{-1} marked with red circles, which is consistent with our experimental observations in Raman measurements. Figure 4(b) shows the relative vibration directions of atoms for A_{1g} and E_{2g} in Fe_3GaTe_2, respectively.[42]

The Raman selection rules show that $E_{2g}(\Gamma)$ appear under co-polarization (XX), cross-polarization (XY) and cross-circular (σ^+ in σ^- out) geometries, while $A_{1g}(\Gamma)$ are active under XX and co-circular (σ^+ in σ^+ out) configurations.[43–47] For XX/XY, the polarization of the incident light is parallel to/perpendicular with the scattered light. Co-circular/cross-circular polarizations present right-handed circular incident light that can be scatted into right/left-handed circular outgoing light, respectively.

The typical Raman spectra of Fe_3GaTe_2 at room temperature under both XX and XY geometries are shown in Fig. 4(c). The prominent phonon mode locating at 155 cm^{-1} could be probed under both XX and XY geometries, while the Raman intensity is strongly decreased for XY configuration. It means that the phonon mode at 155 cm^{-1} should possess two components of $A_{1g}(\Gamma)$ and $E_{2g}(\Gamma)$ simultaneously. The helicity-resolved Raman spectra of the same sample is shown in Fig. 4(d). The peak locating at 155 cm^{-1} appears at both co-circularly and cross-circularly polarized geometry, further indicating the incorporated two $A_{1g}(\Gamma)$ and $E_{2g}(\Gamma)$ components. For A_{1g} single phonon mode, it does not reverse the helicity of the incident photons. It is active under co-circularly geometry with zero angular momenta. In contrast, $E_{2g}(\Gamma)$ phonon at high symmetry Γ point of the Brillouin zone can have nonzero phonon pseudoangular momentum, due to the superposition of the doubly degenerate $E_{2g}(\Gamma)$ modes. The conservation of PAM in the Raman process suggests that $l_s = l_i - l_{ph}$, where l_i, l_s and l_{ph} are the angular momenta of the incident light, scattered light and the phonon, respectively. For the doubly degenerate $E_{2g}(\Gamma)$ chiral phonons, $l_s = 1$ or -1. The PAM is conserved for optical selection rule $\Delta l_{ph} = l_s + 3N$, where Δl_{ph} denotes the change of photon angular momentum and $3N$ represents the azimuthal quantum number of crystal lattice with threefold rotational symmetry. Thus, the process can occur when $l_s(-1) = l_i(+1) - l_{ph}(-1 + 3N)$. In Fig. 4(d), the incident right-handed light (σ^+) can be scattered into left-handed light (σ^-) and chiral phonon $E_{2g}(\Gamma)$ with PAM of -1. Thus, the helicity-resolved Raman scattering in Fig.4(d) can exhibit the chiral (red curve) and non-chiral (blue curve) nature of the $E_{2g}(\Gamma)$ and $A_{1g}(\Gamma)$.

We further carried out magnetic-field dependent Raman characterization at 1.7 K to investigate the magneto-optical effect in the few-layer Fe_3GaTe_2. Figure 4(e) shows the Raman intensity for $E_{2g}(\Gamma)$ and $A_{1g}(\Gamma)$ modes for both XX and XY configurations when tuning the out-of-plane magnetic field from 0 T to 5 T. Raman intensity of $E_{2g}(\Gamma)$ normally do not change with external magnetic field, since E-mode has twofold degeneracy so that the Raman intensity includes two terms that compensate each other under the magnetic field [see Eq. (2)].[43,44] Thus, we deduct the contribution of $E_{2g}(\Gamma)$ mode from the phonon vibrates at 155 cm^{-1}. The extracted Raman intensity evolution of $A_{1g}(\Gamma)$ mode under magnetic field for XX and XY configurations are shown in Fig. 4(f). We define the degree of polarization (DOP) of the Raman intensity as $\frac{I_{XX}-I_{XY}}{I_{XX}+I_{XY}}$. DOP of $A_{1g}(\Gamma)$ mode as a function of applied magnetic field are shown in Fig. 4(g) and Si phonon is also plotted as a reference. DOP of $A_{1g}(\Gamma)$ phonon mode can be modulated from 100% to −35% with the magnetic field changing from 0 T to 5 T. Under negative magnetic field, DOP of $A_{1g}(\Gamma)$ mode exhibits a similar trend of variation, modulated from 100% to −60%, as shown by the blue line in Fig. 4(g). Electrons in the material can experience a Lorentz force, causing an antisymmetric term in the Raman tensor. Nondegenerate A_{1g} Raman tensor is dependent on the magnitude of the magnetic field B [see Eq. (3)]. As a consequence, the prominent DOP variation and giant magneto-Raman effect can be observed in Fe_3GaTe_2. Note that E_{2g} and A_{1g} Raman intensities can be described by the following equations:[43,44]

$$I_{xx}^{E_{2g}} = I_{xy}^{E_{2g}} \propto a^2 \left| \frac{B}{B_0^2 + B^2} \right|^2 + b^2 \left| \frac{B}{B_0^2 + B^2} \right|^2, \quad (2)$$

$$I_{xx}^{A_{1g}} \propto c^2 \left| \frac{B_0}{B_0^2 + B^2} \right|^2, \quad I_{xy}^{A_{1g}} \propto d^2 \left| \frac{B}{B_0^2 + B^2} \right|^2, \quad (3)$$

$$B_0 = \frac{my}{e} \left(1 - i \frac{\omega_0^2 - \omega^2}{\omega \gamma} \right), \quad (4)$$

where a, b, c, and d are parameters of the field independent Raman tensor, B_0 is a resonance-like parameters, determined by electronic mass m, charge e, damping parameter γ, the frequency of the incident light ω, and the restoring frequency of excited electrons ω_0.

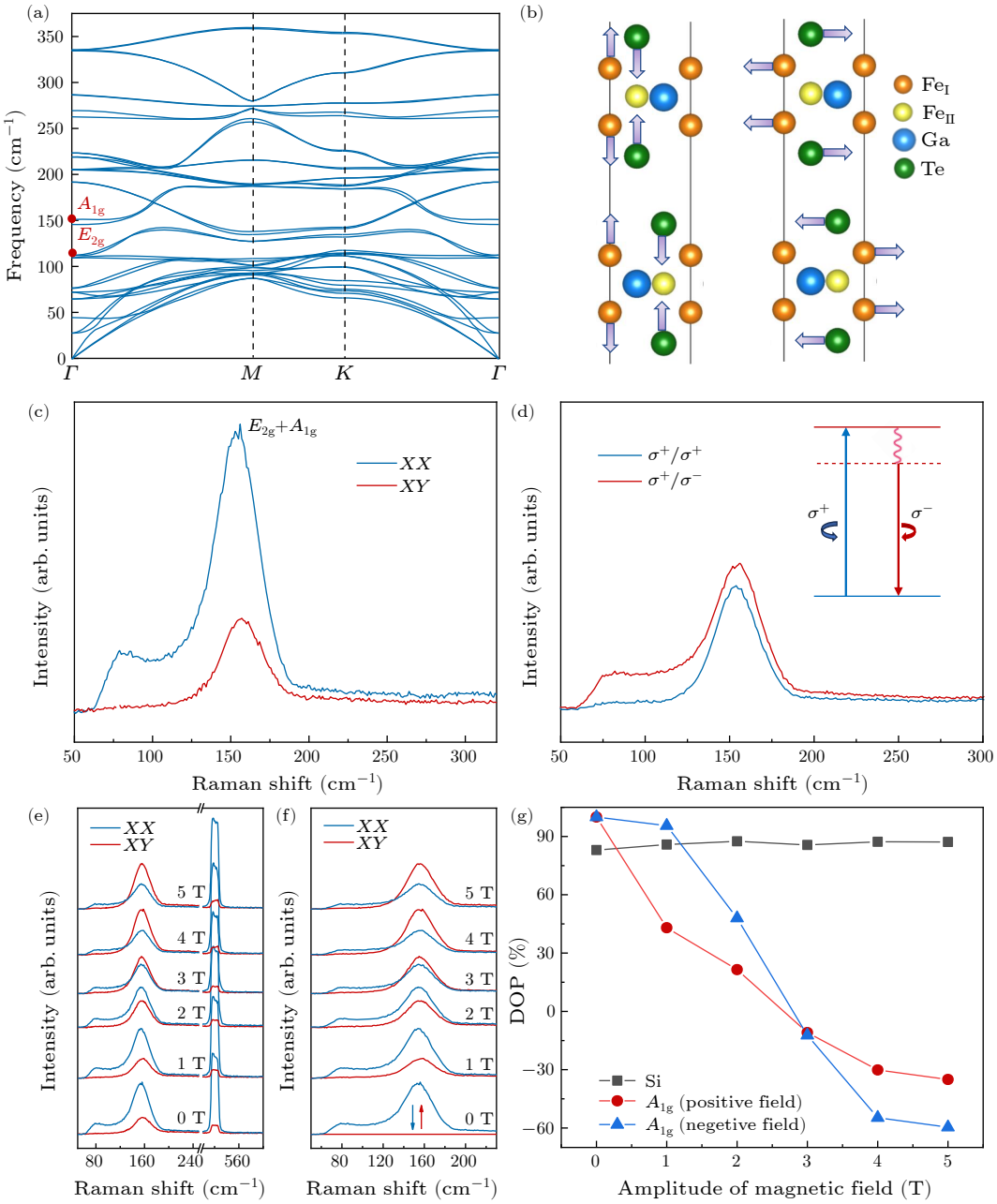

Fig. 4. The chirality of Raman active phonons and magneto-optical Raman effect of Fe_3GaTe_2. (a) First-principles calculation of phonon dispersion band structure based on few-layer Fe_3GeTe_2. The phonon mode branches of A_{1g} and E_{2g} are marked with red circles. (b) The schematic of the A_{1g} (left) and E_{2g} (right) vibrational mode in Fe_3GaTe_2, where the relative vibration direction of the atoms is labeled by the arrows. (c) Raman spectra of Fe_3GaTe_2 at room temperature under both XX (blue) and XY (red) geometries. (d) Helicity-resolved Raman spectra. Inset is the schematic of the helicity of photon switched by the chiral $E_{2g}(\Gamma)$ phonon. (e) Magnetic-field dependent Raman spectra of Fe_3GaTe_2 in co- (blue) and cross-linearly (red) polarized configurations at 1.7 K. (f) The extracted Raman intensity evolution of $A_{1g}(\Gamma)$ mode under magnetic field for XX (blue) and XY (red) configurations. The blue/red arrows show the variation trend of A_{1g} intensity with magnetic field under XX and XY linear polarization. (g) Degree of polarization of A_{1g} of Fe_3GaTe_2 and TO phonon of Si as a function of magnetic field. The blue line represents the result of A_{1g} of Fe_3GaTe_2 under a negative magnetic field, while the red line represents a positive magnetic field.

In summary, we have successfully synthesized high-quality Fe_3GaTe_2 single crystals using the self-flux method. We conduct a series of magnetic-optical characterization to shed light on the intrinsic properties of Fe_3GaTe_2, including RMCD and polarization-resolved Raman characterizations. The results of RMCD are consistent with the AHE results, indicating its excellent PMA and T_C of up to 370 K. Using linearly polarized and helicity-resolved Raman scattering spectroscopy, we demonstrate that the chirality of the E_{2g} phonon mode in Fe_3GaTe_2 2D magnets. The degenerate E_{2g} mode causes the helicity of the incident photons to reverse due to its chiral properties, with a PAM of $l = \pm 1$. When an external out-of-plane magnetic field is applied, the non-chiral A_{1g} mode exhibits a significant magneto-optical Raman effect. Our results provide a solid foundation for understanding new physical phenomena in 2D Fe_3GaTe_2 magnets and offer a basis for future applications of spintronic devices.

Acknowledgments. This work was supported by the National Key Research and Development Program of China (Grant No. 2022YFA1405100), the Beijing Natural Science Foundation Key Program (Grant No. Z220005), and the National Natural Science Foundation of China (Grant Nos. 12241405, 12174384, and 12204058).

References

[1] Gong C, Li L, Li Z, Ji H, Stern A, Xia Y, Cao T, Bao W, Wang C, Wang Y, Qiu Z Q, Cava R J, Louie S G, Xia J, and Zhang X 2017 *Nature* **546** 265

[2] Huang B V, Clark G, Navarro-Moratalla E, Klein D R, Cheng R, Seyler K L, Zhong D, Schmidgall E, McGuire M A, Cobden D H, Yao W, Xiao D, Jarillo-Herrero P, and Xu X D 2017 *Nature* **546** 270

[3] Zhuang H L, Xie Y, Kent P R C, and Ganesh P 2015 *Phys. Rev. B* **92** 035407

[4] Li T X, Jiang S W, Sivadas N, Wang Z F, Xu Y, Weber D, Goldberger J E, Watanabe K, Taniguchi T, Fennie C J, Fai Mak K and Shan J 2019 *Nat. Mater.* **18** 1303

[5] O'Hara D J, Zhu T C, Trout A H, Ahmed A S, Luo Y K, Lee C H, Brenner M R, Rajan S, Gupta J A, McComb D W, and Kawakami R K 2018 *Nano Lett.* **18** 3125

[6] Li B, Wan Z, Wang C, Chen P, Huang B, Cheng X, Qian Q, Li J, Zhang Z W, Sun G Z, Zhao B, Ma H F, Wu R X, Wei Z M, Liu Y, Liao L, Ye Y, Huang Y, Xu X D, Duan X D, Ji W, and Duan X F 2021 *Nat. Mater.* **20** 818

[7] Kim K, Lim S Y, Lee J U, Lee S, Kim T Y, Park K, Jeon G S, Park C H, Park J G, and Cheong H 2019 *Nat. Commun.* **10** 345

[8] Wang Z A, Xue W S, Yan F G, Zhu W K, Liu Y, Zhang X H, Wei Z M, Chang K, Yuan Z, and Wang K Y 2023 *Nano Lett.* **23** 710

[9] Wang Z A, Zhang X M, Zhu W K, Yan F G, Liu P F, Yuan Z, and Wang K Y 2023 *Chin. Phys. Lett.* **40** 077201

[10] Lin H L, Yan F G, Hu C, Zheng Y H, Sheng Y, Zhu W K, Wang Z A, Zheng H Z, and Wang K Y 2022 *Nanoscale* **14** 2352

[11] Zhu W K, Lin H L, Yan F G, Hu C, Wang Z A, Zhao L X, Deng Y C, Kudrynskyi Z R, Zhou T, Kovalyuk Z D, Zheng Y H, Patanè A, Žutić I, Li S S, Zheng H Z, and Wang K Y 2021 *Adv. Mater.* **33** 2104658

[12] Lin H L, Yan F G, Hu C, Lv Q S, Zhu W K, Wang Z A, Wei Z M, Chang K, and Wang K Y 2020 *ACS Appl. Mater. Interfaces* **12** 43921

[13] Hu C, Yan F G, Li Y C, and Wang K Y 2021 *Chin. Phys. B* **30** 097505

[14] Hu C, Zhang D, Yan F G, Li Y C, Lv Q S, Zhu W K, Wei Z M, Chang K, and Wang K Y 2020 *Sci. Bull.* **65** 1072

[15] Zheng Y H, Ma X L, Yan F G, Lin H L, Zhu W K, Ji Y, Wang R S, Wang K Y 2022 *npj 2D Mater. Appl.* **6** 62

[16] Huang B, Clark G, Klein D R, MacNeill D, Navarro-Moratalla E, Seyler K L, Wilson N, McGuire M A, Cobden D H, Xiao D, Yao W, Jarillo-Herrero P, and Xu X D 2018 *Nat. Nanotechnol.* **13** 544

[17] Jiang S, Li L, Wang Z, Mak K F, and Shan J 2018 *Nat. Nanotechnol.* **13** 549

[18] Deng Y J, Yu Y J, Song Y C, Zhang J Z, Wang N Z, Sun Z Y, Yi Y F, Wu Y Z, Wu S W, Zhu J Y, Wang J, Chen X H, and Zhang Y B 2018 *Nature* **563** 94

[19] Li Q, Yang M M, Gong C, Chopdekar R V, N'Diaye A T, Turner J, Chen G, Scholl A, Shafer P, Arenholz E, Schmid A K, Wang S, Liu K, Gao N, Admasu A S, Cheong S W, Hwang C, Li J, Wang F, Zhang X, and Qiu Z Q 2018 *Nano Lett.* **18** 5974

[20] Wang H, Liu Y, Wu P, Hou W, Jiang Y, Li X, Pandey C, Chen D, Yang Q, Wang H, Wei D, Lei N, Kang W, Wen L, Nie T, Zhao W, and Wang K L 2020 *ACS Nano* **14** 10045

[21] Zhang L, Huang X, Dai H, Wang M, Cheng H, Tong L, Li Z, Han X, Wang X, Ye L, and Han J 2020 *Adv. Mater.* **32** 2002032

[22] Idzuchi H, Llacsahuanga Allcca A E, Pan X C, Tanigaki K, and Chen Y P 2019 *Appl. Phys. Lett.* **115** 232403

[23] Cao Y, Zhang X M, Zhang X P, Yan F G, Wang Z A, Zhu W K, Tan H, Golovach V N, Zheng H Z, and Wang K Y 2022 *Phys. Rev. Appl.* **17** L051001

[24] May A F, Ovchinnikov D, Zheng Q, Hermann R, Calder S, Huang B, Fei Z Y, Liu Y H, Xu X D, and McGuire M A 2019 *ACS Nano* **13** 4436

[25] Sun X, Li W, Wang X, Sui Q, Zhang T, Wang Z, Liu L, Li D, Feng S, Zhong S, Wang H, Bouchiat V, Nunez Regueiro M, Rougemaille N, Coraux J, Purbawati A, Hadj-Azzem A, Wang Z, Dong B, Wu X, Yang T, Yu G, Wang B, Han Z, Han X, and Zhang Z 2020 *Nano Res.* **13** 3358

[26] Zhang G J, Guo F, Wu H, Wen X K, Yang L, Jin W, Zhang W F, and Chang H X 2022 *Nat. Commun.* **13** 5067

[27] Zhu W K, Xie S H, Lin H L, Zhang G J, Wu H, Hu T G, Wang Z A, Zhang X M, Xu J H, Wang Y J, Zheng Y H, Yan F G, Zhang J, Zhao L X, Patané A, Zhang J, Chang H X, and Wang K Y 2022 *Chin. Phys. Lett.* **39** 128501

[28] Li W H, Zhu W K, Zhang G J, Wu H, Zhu S G, Li R Z, Zhang E Z, Zhang X M, Deng Y C, Zhang J, Zhao L X, Chang H X, and Wang K Y 2023 *Adv. Mater.* **35** 2303688

[29] Pan Z C, Li D, Ye X G, Chen Z, Chen Z H, Wang A Q, Tian M L, Yao G J, Liu K H, and Liao Z M 2023 *Sci. Bull.* **68** 2743

[30] Ji Y B, Yang S, Ahn H B, Moon K W, Ju T S, Im M Y, Han H S, Lee J S, Park S Y, Lee C G, Kim K J, and Hwang C Y 2024 *Adv. Mater.* **36** 2312013

[31] Strohm C, Rikken G L J A, and Wyder P 2005 *Phys. Rev. Lett.* **95** 155901

[32] Jotzu G, Messer M, Desbuquois R, Lebrat M, Uehlinger T, Greif D, and Esslinger T 2014 *Nature* **515** 237

[33] Kim K, Vetter E, Yan L, Yang C, Wang Z, Sun R, Yang Y, Comstock A H, Li X, Zhou J, Zhang L, You W, Sun D, and Liu J 2023 *Nat. Mater.* **22** 322

[34] Wang C S, Wang J, Xie W Q, Zhang G J, Wu H, Zhou J H, Zhu X D, Ning W, Wang G P, Tan C, Wang L, Du H F, Zhao Y J, Chang H X, Zheng G L, Geng W T, and Tian M L 2023 *Phys. Rev. B* **107** L140409

[35] Fei Z Y, Huang B, Malinowski P, Wang W B, Song T C, Sanchez J, Yao W, Xiao D, Zhu X Y, May A F, Wu W D, Cobden D H, Chu J H, and Xu X D 2018 *Nat. Mater.* **17** 778

[36] Mak K F, Shan J, and Ralph D C 2019 *Nat. Rev. Phys.* **1** 646

[37] Zhang Z D 2007 *Philos. Mag.* **87** 5309

[38] Zang Z H, Zhu Y Z, Xi M, Tian S J, Wang T T, Gu P F, Peng Y X, Yang S Q, Xu X L, Li Y P, Han B, Liu L W, Wang Y L, Gao P, Yang J B, Lei H C, Huang Y, and Ye Y 2022 *Phys. Rev. Lett.* **128** 017201

[39] Jin W C, Kim H H, Ye Z P, Li S W, Rezaie P, Diaz F, Siddiq S, Wauer E, Yang B W, Li C H, Tian S J, Sun K, Lei H C, Tsen A W, Zhao L Y, and He R 2018 *Nat. Commun.* **9** 5122

[40] Peng Y X, Cheng X, Gu P F, Wang F G, Yang J, Xue M Z, Yang W Y, Wang C S, Liu S Q, Watanabe K, Taniguchi T, Ye Y, and Yang J B 2020 *Adv. Funct. Mater.* **30** 1910036

[41] Wang M J, Lei B, Zhu K J, Deng Y Z, Tian M L, Xiang Z J, Wu T, and Chen X H 2024 *npj 2D Mater. Appl.* **8** 22

[42] Gong Y, Hu M, Harris N, Yang Z H, Xie T, Teklu A, Kuthirummal N, Koenemann J, Xu X H, Cheong S W, McLoud W, and Gong C 2022 *npj 2D Mater. Appl.* **6** 9

[43] Ji J T, Zhang A M, Fan J H, Li Y S, Wang X Q, Zhang J D, Plummer E W, and Zhang Q M 2016 *Proc. Natl. Acad. Sci. USA* **113** 2349

[44] Yin T T, Ulman K A, Liu S, Águila A G, Huang Y Q, Zhang L F, Serra M, Sedmidubsky D, Sofer Z, Quek S Y, and Xiong Q H 2021 *Adv. Mater.* **33** 2101618

[45] Du L J, Tang J, Zhao Y C, Li X M, Yang R, Hu X R, Bai X Y, Wang X, Watanabe K J, Taniguchi T, Shi D X, Yu G Q, Bai X D, Hasan T, Zhang G Y, and Sun Z P 2019 *Adv. Funct. Mater.* **29** 1904734

[46] Lyu B, Gao Y F, Zhang Y J, Wang L, Wu X H, Chen Y N, Zhang J S, Li G M, Huang Q L, Zhang N P, Chen Y Z, Mei J W, Yan H G, Zhao Y, Huang L, and Huang M Y 2020 *Nano Lett.* **20** 6024

[47] McCreary A, Mai T T, Utermohlen F G, Simpson J R, Garrity K F, Feng X Z, Shcherbakov D, Zhu Y L, Hu J, Weber D, Watanabe K, Taniguchi T, Goldberger J E, Mao Z Q, Lau C N, Lu Y M, Trivedi N, Valdés Aguilar R, and Hight Walker A R 2020 *Nat. Commun.* **11** 3879